Nematic liquid crystal alignment on chemical patterns

J. P. Bramble[a]; S. D. Evans[a]; J. R. Henderson[a]; C. Anquetil[b]; D. J. Cleaver[b]; N. J. Smith[c]

[a] Molecular and Nanoscale Physics, School of Physics and Astronomy, University of Leeds, Leeds, LS2 9JT [b] Materials Modelling Group, Sheffield Hallam University, City Campus, Sheffield, S1 1WB [c] Sharp Laboratories of Europe Ltd, Oxford, OX4 4GB

PLEASE SCROLL DOWN FOR ARTICLE

Taylor & Francis
Taylor & Francis Group

Nematic liquid crystal alignment on chemical patterns

J.P. BRAMBLE†, S.D. EVANS*†, J.R. HENDERSON†, C. ANQUETIL‡, D.J. CLEAVER‡ and N.J. SMITH§

†Molecular and Nanoscale Physics, School of Physics and Astronomy, University of Leeds, Woodhouse Lane, Leeds, LS2 9JT
‡Materials Modelling Group, Sheffield Hallam University, City Campus, Howard Street, Sheffield, S1 1WB
§Sharp Laboratories of Europe Ltd, Edmund Halley Road, Oxford Science Park, Oxford, OX4 4GB

Patterned Self-Assembled Monolayers (SAMs) promoting both homeotropic and planar degenerate alignment of 6CB and 9CB in their nematic phase were created using microcontact printing of functionalized organothiols on gold films. The effects of a range of different pattern geometries and sizes were investigated, including stripes, circles and checkerboards. Evanescent wave ellipsometry was used to study the orientation of the liquid crystal (LC) on these patterned surfaces during the isotropic-nematic phase transition. Pretransitional growth of a homeotropic layer was observed on 1 μm homeotropic aligning stripes, followed by a homeotropic monodomain state prior to the bulk phase transition. Accompanying Monte Carlo simulations of LCs aligned on nanoscale-patterned surfaces were also performed. These simulations also showed the presence of the homeotropic monodomain state prior to the transition.

1. Introduction

Techniques for patterning substrates on the micrometre scale are now routine in surface science. Some of these methods can readily be used to produce features on the nanoscale. However, almost nothing is known experimentally about liquid crystal (LC) anchoring on patterned substrates when the pattern scale falls below the wavelength of light. In contrast, analogous computer simulation studies, based on simplified molecular models, are most suited to the nanoscale. From such simulations (as presented below) it is evident that LC anchoring due to nanoscale patterning is remarkably similar, qualitatively, to experimental observations at a scale expanded by three orders of magnitude. Simulation and experiment approach the interesting technological scale of 100 nm features from opposite directions. The future should see this gap closed rapidly, such that the extent to which anchoring phenomena at this scale can be directly interpreted in terms of molecular interactions is likely to become a major issue. In this initial study we explore what can already be observed on the length scales most appropriate to the complimentary techniques of experiment and simulation.

Chemical patterning of surfaces for LC alignment also promises to deliver a number of significant advantages for device technology over existing non-patterned surfaces. Such advantages include improved optical performance and wider viewing angles [1, 2] and novel devices such as graded refractive index (GRIN) micro-lenses [3, 4]. Current methods used to pattern surfaces for LC alignment are photoalignment [3–5], micro-rubbing [6], scratching with atomic force microscopy tips [7] and patterned self-assembled monolayers of silanes [8, 9] or alkanethiols on gold [10, 11]. The use of micro-patterning is potentially attractive because the azimuthal and the polar orientation of the LC can be controlled accurately [3, 12].

The behaviour of confined nematic LCs is of fundamental importance for display and switching device applications. Close proximity to a confining substrate clearly breaks the symmetry of the fluid on molecular length scales, inducing phenomena such as positional layering and modified orientational ordering [13]. In LCs, at a continuum level, these effects are described in terms of anchoring [14], in which the substrate is taken to promote one or more preferred bulk director orientation (e.g. planar, tilted or homeotropic). The strength of this substrate-induced orientational pinning is then characterized by two parameters, the polar and azimuthal anchoring coefficients. However, the links between this anchoring description and the many contributing microscopic interfacial interactions are still rather poorly understood.

---

*Corresponding author. Email: s.d.evans@leeds.ac.uk

Whereas conventional uniaxial alignment is sufficient for some applications, more sophisticated, patterned alignment is needed to improve the optical performance of devices, for instance with respect to the viewing angle. Patterned LC alignment raises various questions, such as 'Can tilt be induced and controlled using patterning?' and 'Can patterning give independent control over the two anchoring coefficients?' Kumar *et al.* [15] showed that substrate morphology at sub-µm scales is of great importance in determining LC alignment. Specifically, they concluded that anisotropy in surface morphology of a substrate on a submicrometre length scale can play a defining role in determining the resulting anchoring behaviour. Scharf *et al.* [9] have demonstrated that nanoscale chemical patterning using silanes on silicon can be used to control the azimuthal and polar orientation of the LC E7.

Some displays being developed for the hand-held device market require two optically-distinct stable states. The ZBD (Zenithal Bistable Device) [16, 17] achieves this by using a blazed grating which has stable 'continuous' and 'defect' states. In recent years, much attention has been given to bistable switching in LC devices due to its potential to achieve high display resolution with significantly decreased power consumption. Kim and colleagues [18–20] presented a general approach to establishing in-plane alignment bistability by exploiting the orientational frustration induced by a checkerboard pattern. Lee *et al.* [21] subsequently demonstrated a continuous variation in LC pretilt using a checkerboard pattern comprising regions with orthogonally etched grooves. Bechtold and Oliveira [22] experimentally investigated the equilibrium configuration of the director for a submicrometre-patterned substrate, creating alternating homeotropic and random planar stripes by selectively irradiating a self-assembled monolayer (SAM) with deep ultraviolet light. James *et al.* [23, 24] also studied striped patterns in their modelling of an liquid crystal on silicon (LCOS) device, where the patterning was achieved using high-resolution linear electrodes with rewritable input voltages.

In this study substrates are chemically micropatterned using microcontact printing of organothiols on gold. In sections 2 and 3, we use this approach to study nematic LC anchoring on a variety of pattern geometries. In section 4, we present computer simulation methods which allow one to relate experimentally observed behaviour to idealized intermolecular potentials. In section 5, evanescent wave ellipsometry (EWE) is used to study the SAM/LC interface. It has been shown previously that the Brewster angle can be used to deduce the anchoring orientation of nematic LCs on SAMs of different functional groups and chain lengths

[25, 26]. In this study the same technique is applied to patterned systems and compared with simulations of generic models.

2. Experimental: nematic LC alignment on patterned SAMs

Patterned surfaces have been prepared using microcontact printing of functionalized organothiols on thin gold films. Glass slides were cleaned rigorously with detergent, MilliQ water (Millipore, USA), methanol, piranha etch (30% hydrogen peroxide, 70% sulphuric acid) and finally MilliQ water. The substrates were dried in nitrogen and mounted in a thermal evaporator (Edwards Auto 306). A 3 nm adhesion layer of Cr was deposited, followed by the deposition of a 25 nm Au film. This thickness is sufficient to create a gold film which is continuous but optically transparent. Hence, it is suitable for polarizing microscopy studies. The substrates were rotated during evaporation to ensure there was no anisotropy in the formation of gold grains, which could lead to non-degenerate azimuthal anchoring [27]. Polydimethylsiloxane (PDMS) (Dow Corning Corporation) was prepared for microcontact printing as described by Kumar and Whitesides [28]. The PDMS was well mixed and degassed under vacuum. A silicon wafer, etched with a series of micrometre-sized features was used as a master for the formation of the PDMS stamps. The wafer was silanized, to aid stamp removal, by immersion in a 1% solution of perfluorodecyltriethoxysilane (Fluorochem Ltd) in DCM for 1 hour. For circular structures, masters were made using negative tone photoresist SU8 2010 (Micro Chem Corporation) on glass substrates. These masters were silanized with the same silane via vapour phase deposition. The PDMS material was poured onto the master in a mould and cured at 60°C for 10 hours. After curing, the PDMS was removed and cut into small stamps. A 7 mM ethanolic solution of HS–$(CH_2)_{17}$–$(CF_2)_9$–CF_3 was prepared. The printing surface of the stamp was inked with this solution for a few minutes and then carefully dried with nitrogen. The stamp was then placed onto the gold surface for 2 minutes. The gold surfaces were then immersed in a 3 mM ethanolic solution of 11-mercaptoundecanoic acid, HS–$(CH_2)_{10}$–COOH (Sigma-Aldrich), for 12 hours. This back fills the non-printed regions to produce a two-component patterned surface. The CF_3-terminated SAMs give homeotropic alignment of the LC nCB where $6 \leqslant n \leqslant 9$, and the COOH-terminated SAMs give planar degenerate alignment of the LC nCB where $5 \leqslant n \leqslant 9$ [25, 26].

LC cells were formed with a homeotropic aligning top surface using CF_3 terminated SAMs on gold. Cell gaps

were maintained with two 23 μm thick stripes of polyethylene terephthalate (PET) film (Goodfellow, UK). The samples were heated above the nematic-isotropic transition temperature of the LC investigated and a small amount of LC (Kingston Chemicals, UK) was placed on the patterned surface before the upper surface was placed on top. The samples were then slowly cooled (0.1°C min^{-1}) into the nematic phase.

For EWE studies, two equilateral high index glass (Tih53) prisms (Galvoptics, UK) were cleaned in isopropanol and dried with nitrogen. A 20 nm film of Au was evaporated onto the bases of the prisms. The prisms were then printed with 1 μm stripes of CF$_3$/COOH. Prism A was printed so that the stripes ran parallel to the plane of incidence and Prism B was printed so that the stripes ran perpendicular to the plane of incidence, as depicted in figure 1. Gold slides were prepared with a CF$_3$-terminated SAM as detailed above and used as a lower surface together with PET spacers to form a cell gap of 23 μm. The cells were then filled with 6CB in the isotropic phase. The temperature of the cell was maintained with an accuracy of 0.05°C with a PID controlled Peltier heater and held for 5 minutes before each reading was taken. Heating and cooling data were taken to check for hysteresis and to ensure reliability. A Jobin Yvon UVISEL ellipsometer was used for all EWE measurements. The angular resolution is 0.01° for this system. The wavelength was set to 633 nm to be consistent with previous experiments [25, 26] and the phase modulated ellipsometer was operated in mode III ($A=+45°$, $M=-45°$) [29, 30].

3. Polarizing microscopy

Polarizing microscopy was used to study the alignment of LCs on patterned surfaces. The alignment of 9CB on non-patterned COOH-terminated SAMs is planar degenerate, as seen in figure 2 (a), but if confined to a stripe geometry, the director of the LC is forced to lie parallel to the stripes. Figure 2 (b) shows a polarizing microscopy image of the LC alignment on a single 10 μm stripe of a COOH-terminated SAM surrounded by a CF$_3$-terminated SAM. The sample is rotated 45° relative to the polarizers so that transmission is maximized. A single polarizer was used to show that the alignment was parallel rather than perpendicular to the stripe. The disclination lines seen running across the stripes are identified as domain walls between different splay domains. The domain wall forms into an approximate ring, which runs around the planar stripe [8].

Figure 2 (c) shows an example of the alignment of 9CB on alternating 2 μm stripes, over a large printed area. Again the alignment of 9CB on COOH-terminated regions is planar and consistently oriented along the direction of the stripes. In the regions where the alignment on both surfaces is homeotropic we can see that there is some transmission of light. This is due to a small variation in the midplane zenithal tilt angle θ. The variation in midplane tilt is expected from elastic models of the director configuration in patterned systems [31, 32]. These results demonstrate that patterning surfaces on a relatively large scale can induce an azimuthal orientation to otherwise planar degenerate aligning surfaces. This is in agreement with previous results of LC alignment on surfaces patterned with homeotropic and planar stripes [8]. It is also consistent with recent analytical results where the azimuthal anchoring energy is low for COOH-terminated SAMs [32].

Figure 3 shows alignment of nematic 9CB on a checkerboard pattern. This cell has a homeotropic top surface and a patterned lower surface. The maximum transmission in the planar regions occurs when the checkerboard is orientated parallel to the polarizers. This shows that the azimuthal alignment direction, ϕ, is at $\phi=45°$ to the checkerboard. The planar to homeotropic (PH) square columns are in a splay state, vertically, with planar alignment at $\phi=45°$ to the checkerboard. These appear bright and are coloured green (figure 3, region A). The homeotropic to homeotropic (HH) columns (figure 3, region B) are coloured due to midplane tilt induced by the neighbouring PH regions. These appear yellow with greyish centres. The
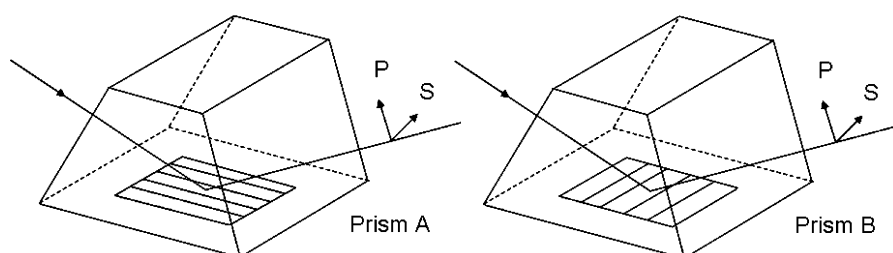

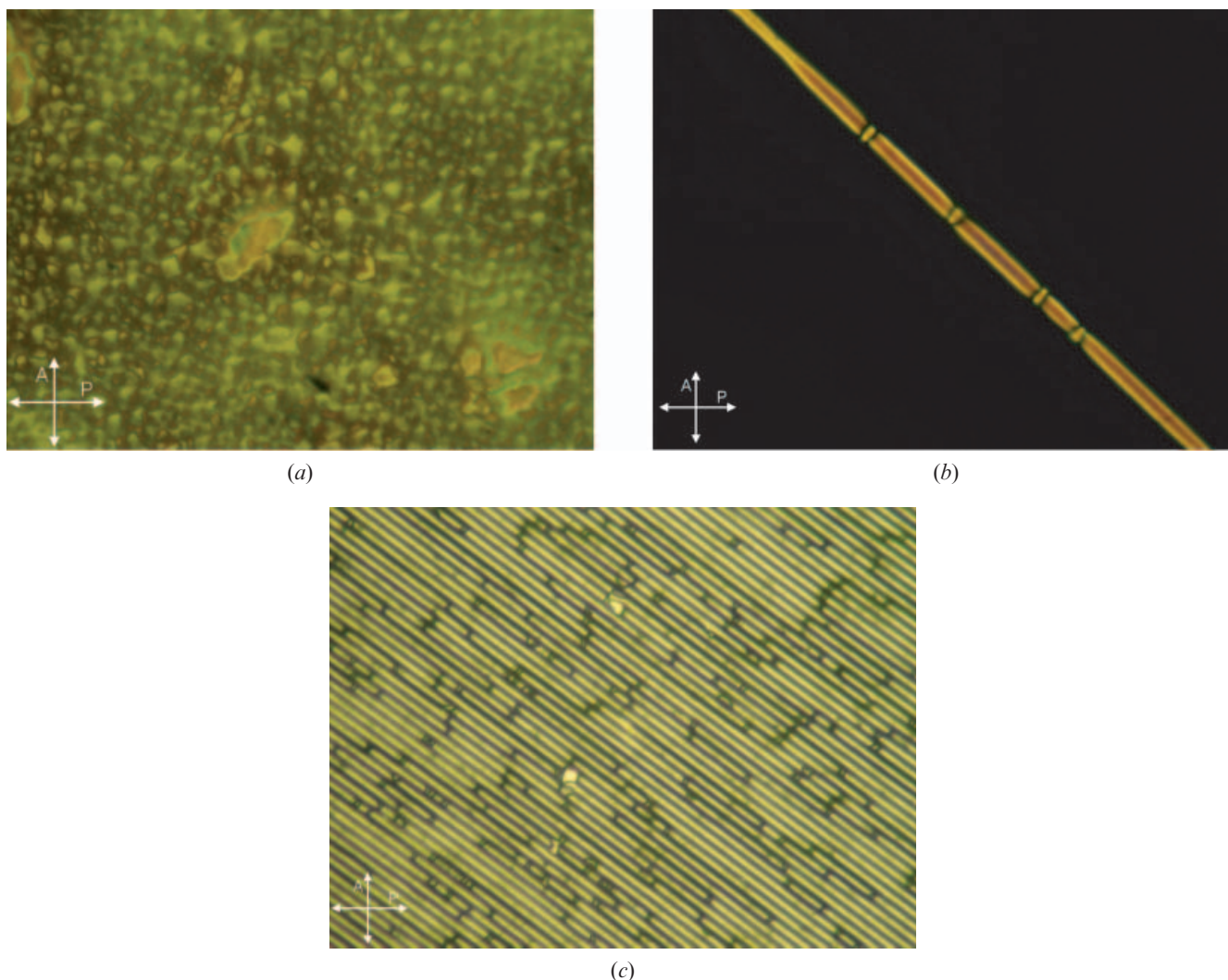Figure 1. Orientation of printing directions for evanescent wave studies.

(a)							(b)

(c)

Figure 2.   Polarizing microscopy images of nematic 9CB aligned on (a) a non-patterned COOH-terminated SAM, (b) a single stripe $10\,\mu m$ wide of COOH-terminated SAM surrounded by a homeotropic aligning CF_3-terminated SAM and (c) $2\,\mu m$ stripes of COOH- and CF_3-terminated SAMS. In the patterned samples the alignment of the planar regions is parallel to the stripe direction.

azimuthal orientation of these regions is also at $\phi=45°$. This image shows two degenerate $\phi=\pm45°$ domains. We can identify them by observing the change in ϕ in the HH regions at the boundary of different PH regions. ϕ changes gradually by $90°$ from one side to the other, so along the diagonal of the square ϕ averages to be parallel to one of the polarizer directions and appears dark (figure 3, region C). Patterned SAMs used as alignment layers differ from other patterning techniques in this respect because the low azimuthal anchoring energy allows these two degenerate states to coexist readily.

Arrays of circular planar aligning regions with a range of diameters were also printed using the approach described above. When the diameter of the circles was $20\,\mu m$ the ordered fluid associated with each circle generally contained nematic threads (figure 4(a)), similar to the alignment seen in non-patterned samples [11]. As the size of the circles was reduced to $10\,\mu m$, the alignment within the circles became symmetrical, with a regular defect structure being seen in virtually all circles (figure 4(b)). The defects are identified as $S=+1$ defects. From the analysis of images of a large number of defects, the ratio of uniform to non-uniform defects can be assessed. Non-uniform defects are identified as circles which contain disordered nematic thread-like textures. For $20\,\mu m$ diameter circles, 39% of the defects were uniform. This increased to 87% uniform defects for $10\,\mu m$ diameter circles. Surface patterning thus provides a route to controlling the size and position of these defects, which could be useful for their study [11, 33].
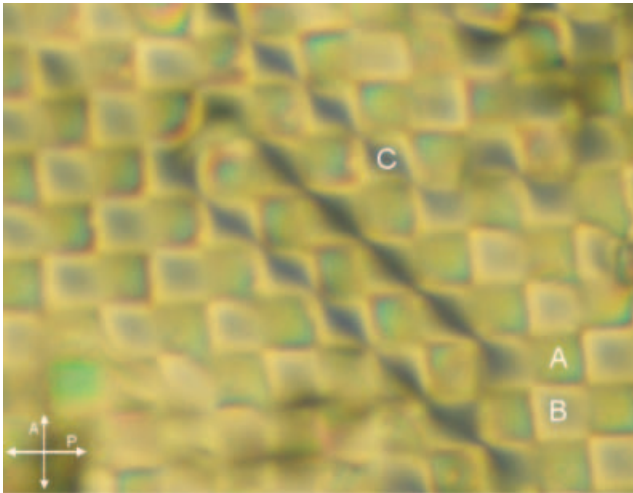
Figure 3. A polarizing microscopy image of nematic 9CB aligned on $16\,\mu m$ squares arranged in a checkerboard pattern consisting of homeotropic aligning CF_3-terminated SAMs and planar aligning COOH-terminated SAMs. The alignment of the planar regions is at $45°$ to the checkerboard. Two degenerate domains are seen. A, a planar to homeotropic region; B, a homeotropic to homeotropic region with polar tilt in the midplane; C, a homeotropic to homeotropic region with a spatially varying value of the azimuthal orientation in the midplane.
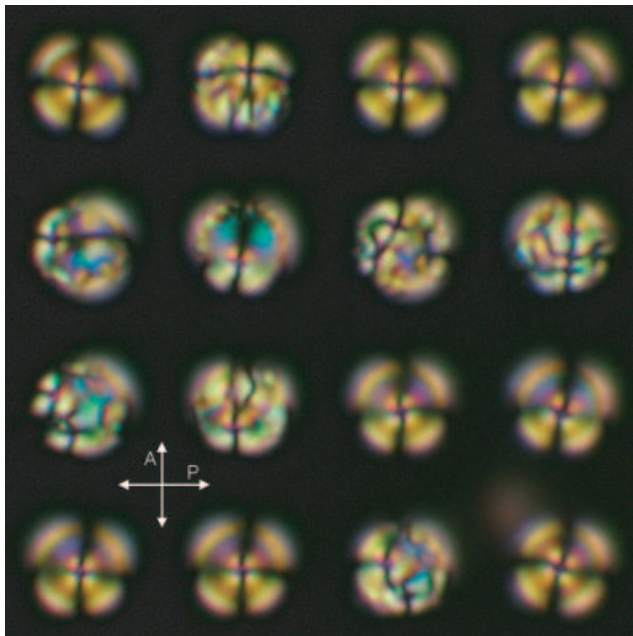
4. Monte Carlo simulations

To complement the experimental work on the micro-metre scale described in the previous section, we have also undertaken a molecular simulation study of LC anchoring at nanoscale-patterned substrates. In this, we have performed a series of Monte Carlo simulations of rod-shaped particles confined in slab geometry between two planar walls. Inter-particle interactions have been modelled through the hard gaussian overlap (HGO) potential [34]. Here, the dependence of the interaction potential v^{HGO} on $\hat{\mathbf{u}}_i$ and $\hat{\mathbf{u}}_j$, the orientations of particles i and j, and $\hat{\mathbf{r}}_{ij}$, the inter-particle unit vector, is
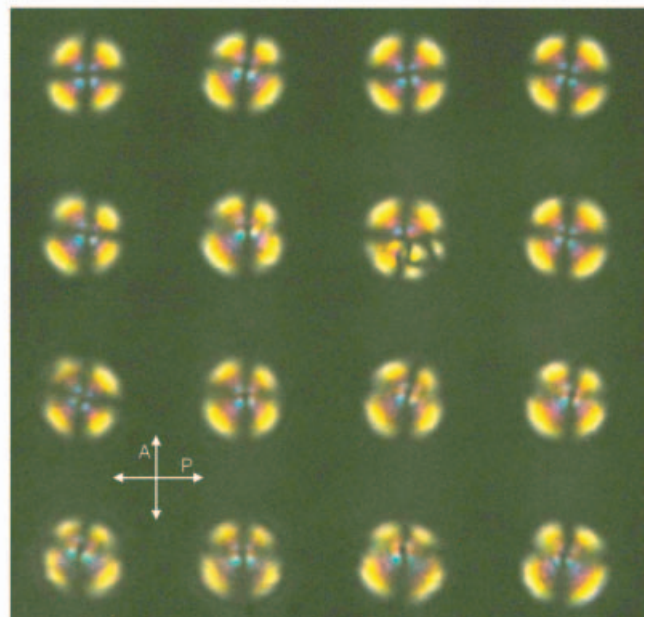
$$v^{HGO} = \begin{cases} 0 & \text{if } r_{ij} \geq \sigma(\hat{\mathbf{r}}_{ij}, \hat{\mathbf{u}}_i, \hat{\mathbf{u}}_j), \\ \infty & \text{if } r_{ij} < \sigma(\hat{\mathbf{r}}_{ij}, \hat{\mathbf{u}}_i, \hat{\mathbf{u}}_j), \end{cases}$$

where $\sigma(\hat{\mathbf{r}}_{ij}, \hat{\mathbf{u}}_i, \hat{\mathbf{u}}_j)$, the contact distance, is given by

$$\sigma(\hat{\mathbf{r}}_{ij}, \hat{\mathbf{u}}_i, \hat{\mathbf{u}}_j) = \sigma_0 \left[1 - \frac{\chi}{2} \left[\frac{(\hat{\mathbf{r}}_{ij} \cdot \hat{\mathbf{u}}_i + \hat{\mathbf{r}}_{ij} \cdot \hat{\mathbf{u}}_j)^2}{1 + \chi(\hat{\mathbf{u}}_i \cdot \hat{\mathbf{u}}_j)} + \frac{(\hat{\mathbf{r}}_{ij} \cdot \hat{\mathbf{u}}_i - \hat{\mathbf{r}}_{ij} \cdot \hat{\mathbf{u}}_j)^2}{1 - \chi(\hat{\mathbf{u}}_i \cdot \hat{\mathbf{u}}_j)} \right] \right]^{-1/2}. \tag{1}$$

(a)

(b)

Figure 4. Polarizing microscopy images of nematic 9CB aligned on circles of planar aligning COOH-terminated SAMs surrounded by homeotropic aligning CF_3 SAMs: (a) $20\,\mu m$ circles; (b) $10\,\mu m$ circles. LC $S=+1$ defects form in the circles and are more stable as the diameter is reduced to $10\,\mu m$.
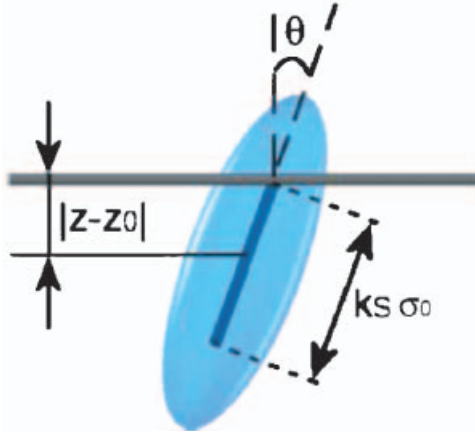
Figure 5. A schematic representation of the geometry used for the HNW particle–substrate interaction [35].

The parameter χ is set by the particle length to breadth ratio $\kappa = \sigma_{end}/\sigma_{side}$ via

$$\chi = \frac{\kappa^2 - 1}{\kappa^2 + 1}. \tag{2}$$

Particle–substrate interactions have been modelled using the hard needle-wall potential (HNW) [35]. In this, the particles do not interact directly with the surfaces. Rather the surface interaction is achieved by considering a hard axial needle of length $\sigma_0 k_s$ placed at

the centre of each particle (see figure 5). This gives an interaction

$$v^{HNW} = \begin{cases} 0 & \text{if } |z_i - z_0| \geq \sigma_w(\hat{\mathbf{u}}_i), \\ \infty & \text{if } |z_i - z_0| < \sigma_w(\hat{\mathbf{u}}_i), \end{cases}$$

where z_0 represents the location of a substrate and

$$\sigma_w(\hat{\mathbf{u}}_i) = \frac{1}{2}\sigma_0 k_s \cos(\theta_i). \tag{3}$$

Here, k_s is the dimensionless needle length and $\theta_i = \arccos(u_{i,z})$ is the angle between the substrate normal and the particle's orientation vector, which also corresponds to the zenithal Euler angle. For small k_s, the homeotropic arrangement has been shown to be stable, whereas planar anchoring is favoured for long k_s [35]. Furthermore, despite its simplicity, the HNW potential has been found to exhibit qualitatively identical behaviour to that obtained using more complex particle–substrate potentials [36]. Here, by imposing variation in k_s across one wall, we investigate the effects of molecular-scale substrate patterning.

All simulations were performed using $N = 864$ HGO particles with a length to breadth ratio $\kappa = 3$. The substrates were separated by a distance $L_z = 4\kappa\sigma_0$ and located at $z_0 = \pm L_z/2$. The simulation box lengths in the other directions were determined, for each imposed value of the dimensionless number density ρ^*, by the relationship $L_x = L_y = \sqrt{N\sigma_0^3/(\rho^* L_z)}$. Typical run lengths at each state point were 0.5×10^6 Monte Carlo
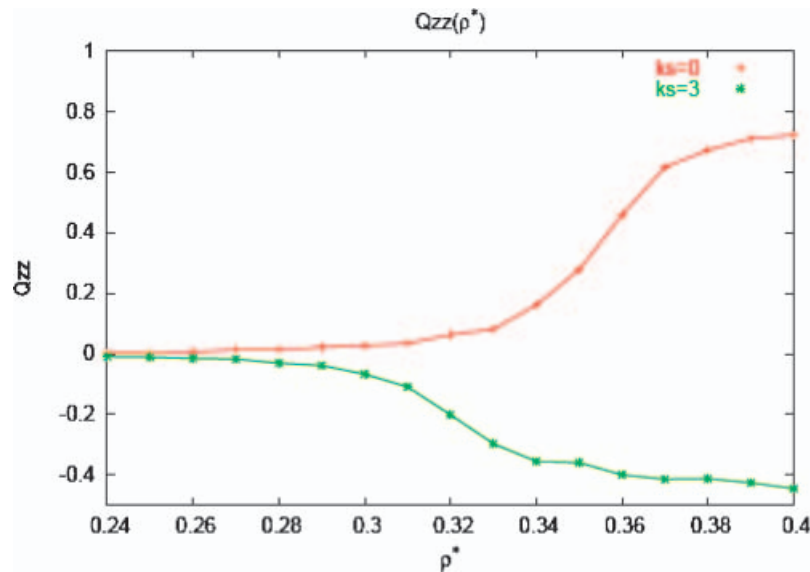

Figure 6. Nematic order parameter measured with respect to the substrate normal, Q_{zz}, for symmetric systems. Here, data values were averaged over the central 50% of the film width.

(a) $\rho^* = 0.24$ (b) $\rho^* = 0.32$ (c) $\rho^* = 0.38$ (d) $\rho^* = 0.40$
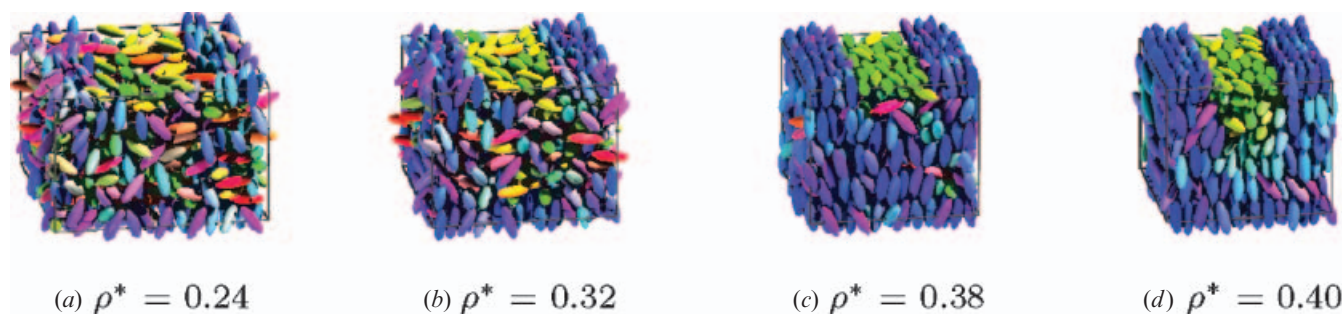
Figure 7. Configuration snapshots from Monte Carlo simulations of striped systems at four reduced densities. Particle colour is used to denote orientation (blue=along z, green=along x, red=along y).

(MC) sweeps (where one sweep represents one attempted move per particle) of equilibration followed by a production run of 0.5×10^6 MC sweeps. Each system studied was compressed from the isotropic phase ($\rho^*=0.24$) into the nematic ($\rho^* \geqslant 0.3$) density range by increasing the number density by $\Delta\rho^*=0.01$ after each production run. Analysis was performed by dividing stored system configurations into 100 equidistant constant-z slices and performing averages of relevant observables in each slice. This yielded profiles of quantities such as $\rho^*(z)$ from which structural changes could be assessed. Orientational order profiles were also measured, particularly

$$Q_{zz}(z) = \frac{1}{N(z)} \sum_{i=1}^{N(z)} \left(\frac{3}{2} u_{i,z}^2 - \frac{1}{2} \right), \qquad (4)$$

which measures variation across the confined films of orientational order measured with respect to the substrate normal. Here $N(z)$ is the instantaneous occupancy of the relevant slice. For patterned systems, we have also further subdivided the system to assess lateral inhomogeneities induced by the patterning.

To characterize the behaviour of our simulated systems we show, in figure 6, the surface normal order induced in non-patterned or symmetric systems. These data correspond to the central region of the symmetric systems, with Q_{zz} values being averaged over the middle 50 layers of our systems. For $k_s=\kappa=3$, negative mid-film Q_{zz} values are observed for $\rho^* \geqslant 0.3$, corresponding to planar anchoring. Conversely, for $k_s=0$, positive Q_{zz} values are seen at high density, indicating homeotropic alignment. The onset of orientational order in the homeotropically anchored system is delayed to higher ρ^* values due to the higher degree of particle adsorption achieved by homeotropically aligned systems.

Having established this baseline behaviour for $\kappa=3$ particles, we have performed an equivalent compression sequence using one unpatterned $k_s=0$ substrate and one striped substrate with k_s set to 0 for half of its area and 3

for the remainder. Here, sharp boundaries are imposed between the different anchoring regions, and the stripe boundaries run parallel to the x-axis of the simulation box. We show, in figure 7, configuration snapshots obtained for this system at four different reduced densities. From these we see that, at the two lower densities, the central region of the film remains relatively disordered, but the near-surface regions adopt orientations consistent with their imposed k_s values. Even at the relatively low density of $\rho^*=0.32$ the particles in the $k_s=3$ stripe show a marked preference to lie parallel to the stripe boundaries. With increase in density, the system becomes dominated by homeotropic alignment, such that at $\rho^*=0.38$ only a thin surface stripe of planar particles is apparent. Rather surprisingly, the influence of the planar surface stripe appears to be greater at the highest density depicted, with the region with planar character appearing to penetrate several particle widths into the system.

In order to assess this interpretation more rigorously, we have calculated density and order parameter profiles for this system. Thus we present, in figures 8 and 9, profiles corresponding to the two distinct y-ranges defined by the imposed stripe pattern. In figure 8, which shows these data for particles confined between two homeotropic substrate regions, the profiles obtained for $\rho^* \leqslant 0.39$ are indistinguishable from the equivalent data obtained from simulations with two unpatterned homeotropic substrates. A qualitative difference is seen on moving to $\rho^*=0.4$, however, since here the value attained in the central section of the Q_{zz} profile decreases with increase in density for the patterned system, whereas (recall figure 6) Q_{zz} increases monotonically with density for symmetric systems with homogeneous alignment. The modified orientational behaviour at high density in this region can be explained by reference to the associated behaviour observed in the second region of the striped substrate system. Here, increase in density leads to an increasingly linear behaviour in the $Q_{zz}(z)$ profile linking the opposing
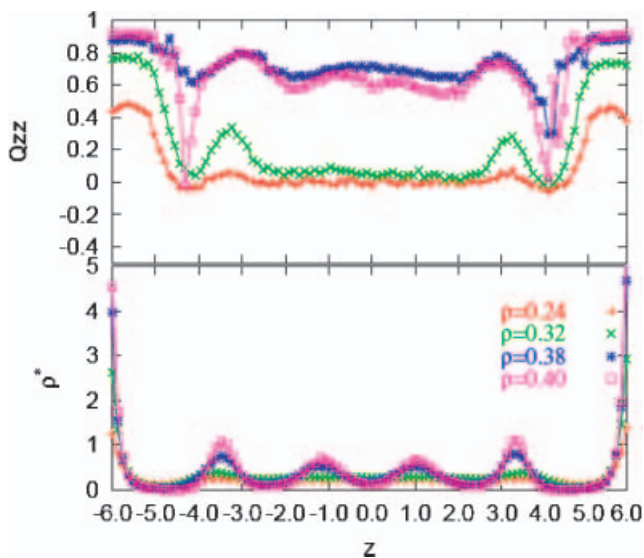
Figure 8. Nematic order parameter and density profile measured with respect to the substrate normal, Q_{zz} and $\rho^*(z)$, for a striped system across the region where $k_s=0$ on both surfaces.

planar and homogeneous substrates. This increased linearity, associated with the adoption of uniform director bend in systems with high orientational order, was noted in a previous investigation by one of the authors of hybrid aligned LC films [35]. We also note, from figure 7, that, away from the immediate vicinity of the patterned substrate, the director and density profiles exhibited by this system vary continuously with y rather
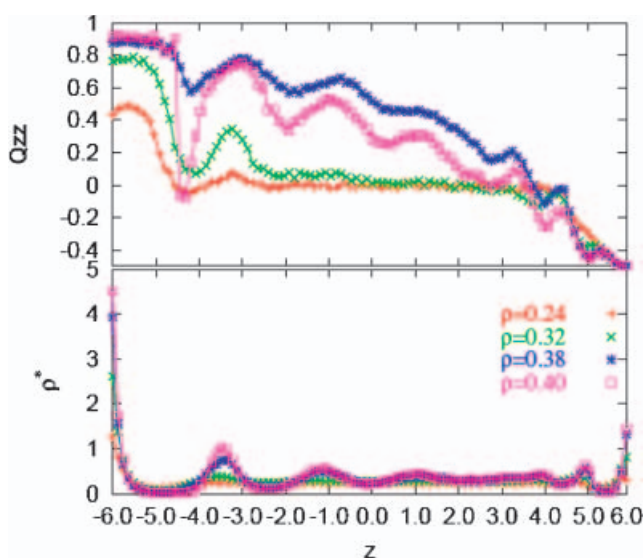

Figure 9. Nematic order parameter and density profile measured with respect to the substrate normal, Q_{zz} and $\rho^*(z)$, for a striped system across the region where $k_s=0$ on the bottom surface and $k_s=3$ on the top surface.

than being strictly divided according to the regimes indicated in figures 8 and 9.

5. Evanescent wave ellipsometry

Data in figure 10 show the change in the Brewster angle as a function of temperature through the nematic–isotropic transition. The diameter of the incident beam was of the order of 1–2 mm, which is significantly greater than the stripe widths, and thus the signal at the detector represents an average over both planar and homeotropic aligning regions. Interestingly, the simulation results in figure 7 explain how the change in the anchoring at the patterned surfaces corresponds to the observed change in the Brewster angle, despite the fact that the simulated system has a periodicity three orders of magnitude smaller.

As the temperature decreases from the isotropic phase, on the right of figure 10, the increasing Brewster angle indicates the pretransitional growth of a homeotropic film at the surface [25, 26]. The decrease in temperature corresponds to increasing density in the simulations, figure 7. This film cannot form on the COOH regions so must form on the CF_3 regions (figure 7 (b)). The average film thickness increases logarithmically as the temperature decreases towards the bulk phase transition at T_{IN}, indicating complete orientational wetting at the patterned surface [25]. The LC on the COOH region should still be isotropic at this point, because planar anchoring does not wet a COOH isotropic surface [25] but the thickness of this region decreases close to the bulk transition due to the encroachment of the homeotropically aligned film from the opposite surface. The peak in the curve indicates that homeotropic anchoring, in the probed region, dominates as $T \to T_{IN}$ (figure 7 (c)); this is the homeotropic monodomain. Beyond this peak the curve then falls, as LC on the COOH region switches from isotropic to planar alignment. The probed region is now a more complex LC structure, consisting of homeotropic and planar aligned regions (figure 7 (d)). The Brewster angle continues to increase at lower temperatures due to the increasing nematic order parameter, in both the homeotropic and planar regions. The final values of the Brewster angle for the two cells are different due to the different alignments of the stripes with respect to the incident light. This is also consistent with our finding that the planar alignment at the surface is oriented along the stripes and not orthogonal to them.

Traditional LC phase gratings employ micropatterned electrodes to create LC structures which have an alternating pattern of non-switched homeotropic and switched Hybrid Aligned Nematic (HAN) LC states [37]. These devices are used in transmission mode and
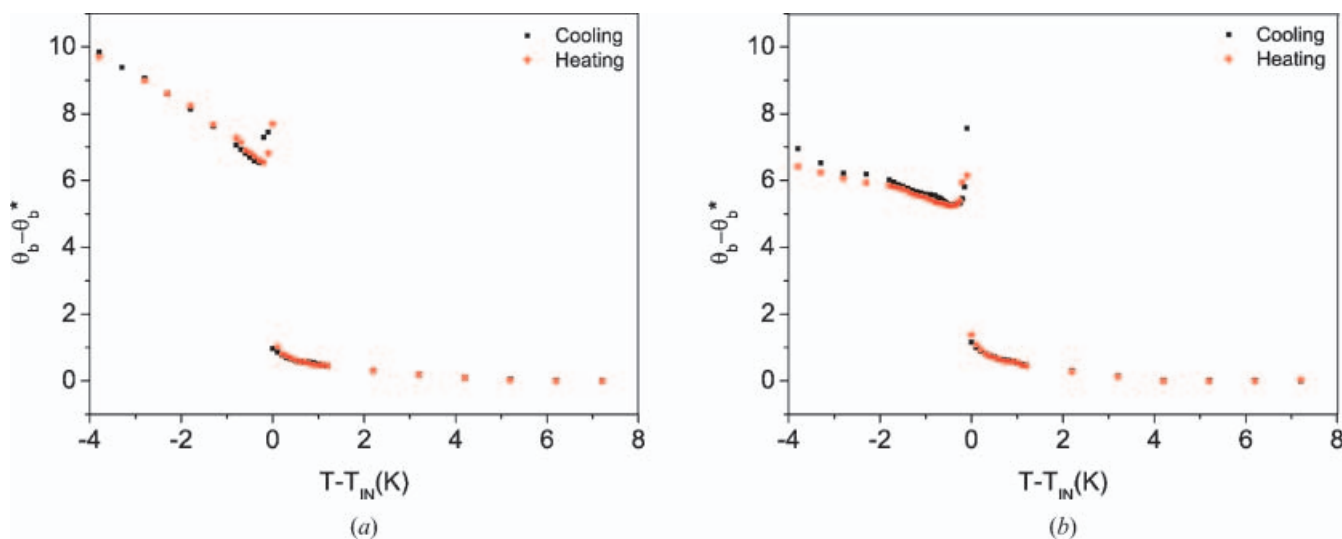
Figure 10. EWE data for a LC/patterned SAM interface: (a) Prism A; (b) Prism B. See figure 1.

the optical phase shift of the LC above the switchable components is proportional to the voltage applied. In the EWE experiment the SAM micropatterned surface creates a LC phase grating due to the difference in the phase of the reflected light from each component, so we can use the intensity of the diffracted beam to verify the anchoring orientation as the temperature is varied through the isotropic–nematic transition. A one-dimensional optical model was used to model ellipsometry measurements of the Prism/Au/LC interface. The model is based on a modified Berreman 4×4 matrix method [38–42].

It can be shown that for a binary phase grating with equal stripe width, the first-order intensity, I, is dependant on the reflection coefficients, R, and ellipsometric phase difference, Δ, between the two components,

labelled P and H, [43],

$$I = \left(\frac{1}{\pi^2}\right)\left(R_P^2 + R_H^2 - 2R_P R_H \cos(\delta\Delta)\right) \quad (5)$$

where $\delta\Delta = \Delta_P - \Delta_H$.

Figure 11 shows the first-order diffraction pattern from cell A. Instead of tracking the Brewster angle we can fix the position of the incident beam and observe the intensity of the diffracted beam. The intensity displays the same four distinct regions of behaviour observed in the Brewster angle data. In the isotropic phase there is clearly no difference in Δ from the two components and the intensity is zero. As $T \to T_{IN}$ the efficiency of the grating increases as the thickness of the homeotropically aligned LC increases on the CF_3 regions. This is analogous to a traditional reflection phase grating becoming deeper. Figure 12 shows the calculated efficiency of the grating as the thickness of the homeotropic region increases. The maximum efficiency obtainable is 1.5%. This is seen experimentally as a gradual increase in brightness with a maximum experimental efficiency of 1.5%. At the peak in our Brewster angle data, the majority of the probed region is homeotropic, this is seen experimentally as a drop in the brightness of the diffracted beam. When the LC on the planar region switches from isotropic to planar, there is a large increase in intensity as the phase difference between the two components is much larger. The maximum theoretical efficiency is now 30%. Note that the modelling assumes perfect order in the LC.
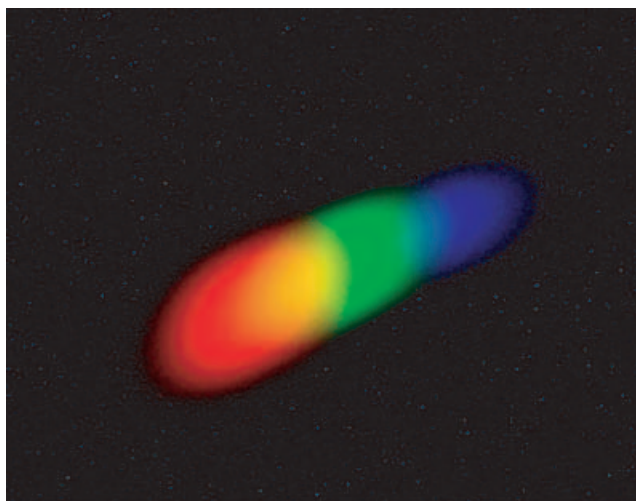

Figure 11. First-order diffraction pattern from cell A.

6. Discussion

We have shown that SAMs of organothiols on gold, patterned in different geometries can be used to control
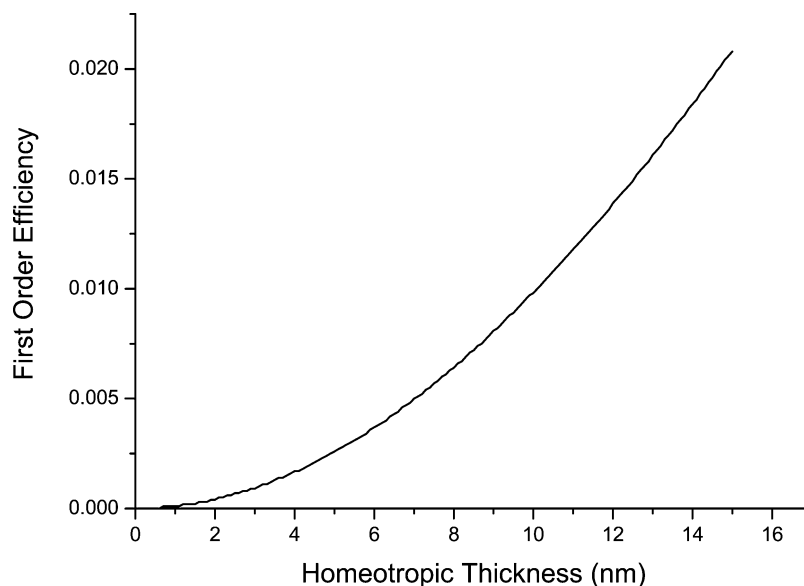
Figure 12. Calculated first-order diffraction efficiency for binary LC phase grating with components of isotropic LC and increasing homeotropic thickness. Calculated at an angle of incidence of 75°.

the formation of LC alignment states and defects. Whilst unpatterned COOH-terminated SAMs give planar degenerate alignment, homeotropic and planar patterning introduces uniform alignment in the planar regions. In the stripe geometry, the LC aligns parallel to the stripes for all scales investigated. This was shown using polarizing microscopy and evanescent wave ellipsometry. The checkerboard geometry creates degenerate, bistable states at 45° to the checkerboard, due to the intrinsic low azimuthal anchoring of the surface. Circular planar regions promote the formation of stable, singular defect structures when the circle diameter is 10 μm or less.

EWE has been used to study the nematic–isotropic transition of nCB on patterned SAMs for the first time. Building on previous results, we see that nCB LCs can orientationally wet homeotropically aligning regions of a surface but not adjacent planar aligning regions. This is seen on patterned systems as small as 1 μm length scales. A homeotropic monodomain is observed on patterned systems prior to the bulk phase transition, however, which causes the efficiency of the LC phase grating to fall to zero. Despite the significantly different length scales involved, the qualitative behaviour seen in Monte Carlo simulations of generic molecular models confined using a striped interface is entirely consistent with the experimental observations. Preliminary EWE experiments on broader stripes of width 10 μm show no homeotropic monodomain around the transition. This suggests that the qualitative behaviour shown by the

Monte Carlo simulations for molecular-scale patternings continues up to a patterning length scale of between 1 and 10 μm.

LC phase gratings have the potential to be of general interest as they offer routes to several different behaviours while remaining a low-cost printing technique. The phase gratings are also switchable if an electric field is applied between the gold films. Further work is now being undertaken to both examine these affects and investigate the behaviours achievable from more sophisticated patterning arrangements.

Acknowledgments

References

[1] J. Chen, P.J. Bos, D.R. Bryant, D.L. Johnson, S.H. Jamal, J.R. Kelly. *Appl. Phys. Lett.*, **67**, 1990 (1995).
[2] M. Schadt, H. Seiberle, A. Schuster. *Nature*, **381**, 212 (1996).
[3] N.J. Smith, P. Gass, M. Tillin, C. Raptis, D. Burbridge. *Sharp Technical J.*, **24**, 5 (2005).
[4] N.J. Smith, P. Gass, J.P. Bramble, M.D. Tillin, B.M. Musgrave. Patent No. GB2411735 (2005).
[5] M. O'Neill, S.M. Kelly. *J. Phys. D: Appl. Phys.*, **33**, R67 (2000).

[6] S. Varghese. *Adv. Mater.*, **16**, 1600–1605 (2004).

[7] J.-H. Kim, M. Yoneya, H. Yokoyama. *Nature*, **420**, 159 (2002).

[8] B.-W. Lee, N. Clark. *Science*, **291**, 2576 (2001).

[9] T. Scharf, S. Park, C. Padeste, H. Schift, N. Basturk, J. Grupp. *Mol. Cryst. Liq. Cryst.*, **55**, 1619 (2005).

[10] R.D. Drawhorn, N.L. Abbott. *J. Phys. Chem.*, **99**, 16511 (1995).

[11] Y.L. Cheng, D.N. Batchelder, S.D. Evans, J.R. Henderson, J.E. Lydon, S.D. Ogier. *Liq. Cryst.*, **27**, 1267–1275 (2000).

[12] T.A. Wilderbeek, F.J.A. van der Meer, K. Feldman, D.J. Broer, C.W.M. Bastiannsen. *Adv. Mater.*, **14**, 655 (2002).

[13] R.G. Horne, J.N. Israelachvili, E. Perez. *J. Phys.*, **42**, 39 (1981).

[14] B. Jerome. *Rep. Progr. Phys.*, **54**, 391–451 (1991).

[15] S. Kumar, J.H. Kim, Y. Shi. *Phys. Rev. E*, **94**, 077803 (2005).

[16] G.P. Bryan-Brown, C.V. Brown, J.C. Jones. US Patent No. 6,249,332 (2001).

[17] J.C. Jones, S. Beldon, E. Wood, P. Brett, M. Francis, M. Goulding. *SID Symp. Digest Technical Papers*, **34**, 954 (2003).

[18] J.H. Kim, M. Yoneya, J. Yamamoto, H. Yokoyama. *Appl. Phys. Lett.*, **78**, 3055 (2001).

[19] M. Yoneya, J.H. Kim, H. Yokoyama. *Appl. Phys. Lett.*, **80**, 374 (2002).

[20] J.H. Kim, M. Yoneya, H. Yokoyama. *Appl. Phys. Lett.*, **83**, 3602 (2003).

[21] F.K. Lee, B. Zhang, P. Sheng. *Appl. Phys. Lett.*, **85**, 5556 (2004).

[22] I.H. Bechtold, E.A. Oliveira. *Liq. Cryst.*, **32**, 343 (2005).

[23] R. James, F.A. Fernandez, S.E. Day. *Mol. Cryst. Liq. Cryst.*, **422**, 209 (2004).

[24] R. James, M.C. Gardner, F.A. Fernandez, S.E. Day. *Mol. Cryst. Liq. Cryst.*, **450**, 105 (2006).

[25] B. Alkhairalla, H. Allinson, N. Boden, S.D. Evans, J.R. Henderson. *Phys. Rev. E*, **59**, 3033 (1999).

[26] B. Alkhairalla, N. Boden, E. Cheadle, S.D. Evans, J.R. Henderson, H. Fukushima, S. Miyashita, H. Schonherr, G.J. Vancso, R. Colorado Jr, M. Graupe, O.E. Shmakova, T.R. Lee. *Europhys. Lett.*, **59**, 410 (2002).

[27] V.K. Gupta, N.L. Abbott. *Langmuir*, **12**, 2587 (1996).

[28] A. Kumar, G.M. Whitesides. *Appl. Phys. Lett.*, **63**, 2002 (1993).

[29] R.M.A. Azzam, N.M. Bashara. *Ellipsometry and Polarised Light*. North-Holland, Amsterdam (1977).

[30] O. Acher, E. Bigan. *Rev. Sci. Instrum.*, **60**, 65 (1989).

[31] G. Barbero, T. Beica, A.L. Alexe-Ionescu, R. Moldovan. *J. Phys. II*, **2**, 2011–2024 (1992).

[32] T.J. Atherton, J.R. Sambles. *Phys. Rev. E*, **74**, 022701 (2006).

[33] C. Satiro, F. Moraesa. *Eur. Phys. J. E*, **20**, 173 (2006).

[34] P. Padilla, E. Velasco. *J. Chem. Phys.*, **106**, 10299 (1997).

[35] D.J. Cleaver, P.I.C. Teixeira. *Chem. Phys. Lett.*, **338**, 1 (2001).

[36] F. Barmes, D.J. Cleaver. *Phys. Rev. E*, **69**, 061705 (2004).

[37] C.V. Brown, Em.E. Kriezis, S.J. Elston. *J. Appl. Phys.*, **91**, 3495 (2002).

[38] D.W. Berreman. *J. Opt. Soc. Am.*, **62**, 502 (1972).

[39] H. Wohler, M. Fritsch, G. Haas, D.A. Mlynsk. *J. Opt. Soc. Am. A*, **5**, 1554 (1988).

[40] P. Yeh. *Optical Waves in Layered Media*. Wiley, New York (1988).

[41] H. Wohler, M. Fritsch, G. Haas, D.A. Mlynsk. *J. Opt. Soc. Am. A*, **8**, 536 (1991).

[42] M. Schubert. *Phys.Rev.B*, **53**, 4265 (1996).

[43] M. Margelevicius, V. Grigaliunas, H. Pranevicius, J. Margelevicius. *Appl. Math. Model.*, **27**, 1035 (2003).